International Journal of Heat and Mass Transfer 93 (2016) 186–199

Contents lists available at ScienceDirect

International Journal of Heat and Mass Transfer

journal homepage: www.elsevier.com/locate/ijhmt

Heat transfer enhancement using rectangular vortex promoters in confined quasi-two-dimensional magnetohydrodynamic flows

Oliver G.W. Cassells, Wisam K. Hussam, Gregory J. Sheard *

Department of Mechanical and Aerospace Engineering, Monash University, VIC 3800 Australia

ARTICLE INFO

Article history:
Received 7 May 2015
Received in revised form 24 September 2015
Accepted 5 October 2015

Keywords:
MHD
Quasi 2D
Hartmann
Vortex promoter
Duct flow
Channel flow
Heat transfer enhancement

ABSTRACT

Heat transfer efficiency from a duct side-wall in which an electrically conducting fluid flows under the influence of a transverse magnetic field is investigated. A quasi-two-dimensional magnetohydrodynamic model is employed to model the flow using high-resolution numerical simulation. The gap height and angle of attack of a rectangular cylinder, with aspect ratio $\alpha = 1/2$ and blockage ratio $\beta = 1/4$, are independently varied to establish relationships between obstacle configuration and heat transfer efficiency. The heat transfer efficiency is measured through an efficiency index given by the ratio of heat transfer enhancement to pressure drop penalty in comparison to an empty duct case. At gap height ratios $1.15 \leqslant G/L_c < 2$ for an upright cylinder above a heated lower wall, thermal enhancement and efficiency can be improved; with a peak thermal efficiency of $\eta = 1.6$ occurring at $G/L_c = 1.5$. Additional increases in thermal efficiency for an obstacle at the duct centre-line ($G/L_c = 2$) can be achieved through inclining the cylinder at $\gamma = -7.5^\circ$, $\gamma = -37.5^\circ$ and $0^\circ < \gamma \leqslant 22.5^\circ$. However, these configurations offered no improvement over simply offsetting an upright cylinder at a gap height ratio of $G/L_c = 1.5$. For a cylinder offset at $G/L_c = 1.5$, varying the incidence angle through $-37.5^\circ < \gamma \leqslant 22.5^\circ$, $-7.5^\circ \leqslant \gamma < 0^\circ$ and $0^\circ < \gamma \leqslant 15^\circ$ can lead to additional thermal efficiency benefits; with a global peak efficiency of $\eta = 1.7$ occurring at $\gamma = -37.5^\circ$. The streamwise distribution of the local time-averaged Nusselt number and the effect of Hartmann dampening for $100 \leqslant Ha \leqslant 2000$ on heat transfer and flow dynamics are also investigated. A net power balance analysis reveals that in fusion applications the heat transfer enhancement dominates over the pumping power cost to produce net benefits for even modest heat transfer enhancement.

1. Introduction

Magnetohydrodynamic (MHD) flow in the presence of a transverse magnetic field occurs within the liquid metal cooling blankets surrounding magnetically confined fusion reactor plasma. Liquid metals moving under the influence of magnetic fields are subjected to electro-magnetic 'Lorentz' forces due to interactions with motion-induced electric currents [1]. Research on such flows has shown that for sufficiently strong transverse magnetic fields, velocity differentials in perpendicular planes are strongly suppressed, while vortices also become elongated and aligned with the magnetic field [1,2]. Duct walls normal to the magnetic field are subjected to the formation of boundary layers, known as Hartmann layers, which exert frictional forces on the internal core flow. For heat intensive applications, such as fusion reactor cooling blankets, this suppression of turbulent structures is detrimental to the operational efficiency, where the removal of large amounts of thermal energy is required [3]. A quasi-two-dimensional (Q2D) model can be constructed to investigate these flows by augmenting the two-dimensional Navier–Stokes equations with additional forcing and linear braking terms, representing the Lorentz forces and friction in the Hartmann layers, respectively [4].

For confined MHD flows in the absence of natural convection effects and turbulence, the validity of the quasi-two-dimensional model is only ensured when there is a sufficiently strong magnetic field (i.e. $Ha \gg 1$), the interaction parameter N, characterising the ratio of electromagnetic to inertial forces, is much greater than unity (i.e. $N = Ha^2/Re \gg 1$), and the scale of the flow structures are larger than the thickness of the out-of-plane duct wall velocity boundary layers (known as a Shercliff layers) [4,5]. Theoretical and experimental research has shown that three-dimensional instabilities in both the Shercliff layers and interior flow do exist even for large interaction parameters [4,6–11]. *Weak* homothetic forms of three dimensionality due directly to the presence of the Hartmann layers can occur in confined MHD flows for all but the highest

* Corresponding author.
E-mail address: Greg.Sheard@monash.edu (G.J. Sheard).

http://dx.doi.org/10.1016/j.ijheatmasstransfer.2015.10.006
0017-9310/

Nomenclature

a	duct depth (out-of-plane)
B	uniform out-of-plane magnetic field strength
c_p	constant pressure specific heat capacity
$C_{d,p}$	cylinder pressure drag coefficient (x-direction)
$C_{d,v}$	cylinder viscous drag coefficient (x-direction)
C_l	cylinder lift coefficient (transverse y-direction)
Ec	Eckert number
G	gap between cylinder centroid and heated duct wall
h	duct height (in the y-direction)
h_c	cylinder cross-section short side length
H	magnetohydrodynamic friction parameter
Ha	Hartmann number
HR	heat transfer enhancement ratio, Nu/Nu_0
L_{duct}	length of duct ($L_u + L_d$)
L_c	cylinder rectangular cross-section long side length
L_d	downstream length of duct (from cylinder centroid)
L_u	upstream length of duct (from cylinder centroid)
$\mathcal{L}^2$	integral of square of velocity magnitude over computational domain
n	number of out-of-plane Hartmann layers (here $n = 2$)
N_p	element polynomial degree
Nu	time-averaged Nusselt number
Nu_0	Nu for the same duct without a cylinder
Nu_w	local Nusselt number along heated side-wall
p	pressure
P	power
Pe	Peclet number
PR	pressure drop penalty ratio, $\Delta p/\Delta p_0$
Pr	Prandtl number
Re	Reynolds number (based on $h/2$)
Re_m	magnetic Reynolds number
t	time
T	temperature scalar
T_f	bulk fluid temperature
T_o	temperature at cold inlet and top wall
T_w	temperature at hot wall
u	horizontal velocity component
u_{avg}	area-averaged horizontal velocity in duct
$\mathbf{u}$	quasi-two-dimensional velocity vector
U_0	peak fluid velocity at duct inlet
x	Cartesian coordinate (streamwise direction)
y	Cartesian coordinate (transverse direction)
z	Cartesian coordinate (vertical out-of-plane direction)

Greek symbols

α	cylinder cross-section aspect ratio
β	blockage ratio
γ	incidence angle
δ_s	Shercliff layer thickness (on duct side-walls)
ΔP	difference in power
Δp	total pressure drop from inlet to outlet
Δp_0	Δp for the same duct without a cylinder
Δt	time step size (numerical time integration)
ΔT	reference temperature difference, $T_w - T_o$
η	efficiency index, HR/PR
κ	fluid thermal diffusivity
ν	fluid kinematic viscosity
ρ	fluid density
σ	electrical conductivity of the fluid
ϕ	heat flux through heated duct side-wall
ψ	Fisher–Pearson third moment coefficient of skewness
ω	Fourier spectra frequency

magnetic field regimes. In addition, *strong* forms of MHD three-dimensionality, where only partial vortex pairing results, does occur for low Ha values [7]. Furthermore, [10] has demonstrated discrepancies between three- and two-dimensional models for interaction parameters up to $N \approx 16$. In contrast, recent research using two- and three-dimensional MHD models has shown that for high Re flows, laminarisation of the Shercliff layers still occurs for sufficiently high Hartmann numbers. Numerical work by [9] found laminarisation of the Shercliff layers at Hartmann numbers greater than 400. Furthermore, [12] demonstrated for low Re flows, three-dimensional instabilities vanished in the Shercliff layers for $Ha \geqslant 65.25$. Numerical work by [17] has also showed that modelling of vortex decay behaviour using the Q2D model is in good agreement with three-dimensional simulation data. Moreover, the quasi-two-dimensional model employed in this work has been shown to provide similar thickness scaling, instabilities, friction and turbulence behaviour to three-dimensional MHD flows [4,13–17].

Due to the dampening of velocity fluctuations along the direction of the magnetic field, longitudinal vortices are dissipated rapidly and transverse vortex generation is thus considered the most viable vortex orientation for heat transfer enhancement in ducted MHD flows [6,18,19]. Heat transfer enhancement using internal obstacles to induce transverse vortices in MHD flows has been the subject of investigation in numerous studies [19,20,22–24]. Research by [20] focused on numerically investigating the effect of Prandtl number and interaction parameter on heat transfer characteristics around a heated static circular cylinder. Furthermore, [24] focused on the effect of Reynolds number and magnetic field strength on free surface MHD flow and heat transfer behaviour around a circular cylinder. An investigation of optimal disturbances maximising energy growth in quasi-two-dimensional flow around a cylinder in a duct by [25] provided insight into the effect of Hartmann number and channel blockage on the amplification of disturbances in the vicinity of the obstacle. Subsequently, [26] promoted instability in a similar duct flow by torsionally oscillating a cylinder resulting in enhancement of heat transfer.

Few studies have investigated the variation of geometric parameters in MHD channel flow on heat transfer characteristics [19,21–23]. [19] showed that only bars placed parallel to the magnetic field aided in increasing the achievable Nusselt number in a channel flow with a heated upper wall for a variety of interaction parameters. A quasi-two-dimensional MHD numerical simulation by [22] showed that the transition from steady to unsteady flow regimes, and in turn thermal characteristics, are a function of Hartmann number and blockage ratio. Following on from the work by [22], [23] showed that there is an optimal gap height above a heated wall at which a circular cylinder should be placed to maximise heat transfer efficiency for certain blockage ratios. This optimal spacing was found to be between approximately 1 and 1.5 times the characteristic length of the obstacle. The thermal response was also shown to be a stronger function of blockage ratio than Reynolds number for a given magnetic field strength. At this location, wake vortices are cast close enough to the heated wall to enhance mixing between low and high temperature fluids, but are still cast high enough to prevent vortex suppression caused by interaction with the Shercliff layers. [21] studied the effect of Hartmann and Reynolds number on heat transfer and vortex dynamics for a square obstacle placed in a quasi-two-dimensional MHD channel. Their results showed the development of a fourth flow regime unlike that observed for hydrodynamic flows, where entrainment of the Shercliff boundary layers leads to greater flow

irregularity and increased rates of heat transfer from a heated sidewall. Furthermore, transition to unsteady regimes was found to occur at lower critical Reynolds numbers for square vortex promoters in comparison to their circular counterparts.

In contrast to the current literature on MHD flows, there has been a vast array of hydrodynamic channel flow investigations which have focused on improving thermal responses using flow disturbance generating devices, such as cylinders, ribs, winglets and baffles. An extensive synopsis of these variegated studies has been documented in reviews for heat transfer applications such as [27,28]. Most pertinent to the methodology of the current study, [29] numerically investigated the effect of vortex promoter shape, angle of attack, aspect ratio and blockage ratio for low *Re* two-dimensional hydrodynamic flows on the heat transfer characteristics from a heated lower wall. Notably the study found superior improvement when changing the vortex promoter geometry in comparison to blockage ratio. Furthermore, thermal efficiency improvement was found to be more strongly dependent on incidence angle than on position relative to the channel centre-line. On the balance of manufacturability and performance, the authors concluded that an inclined rectangular vortex promoter with aspect ratio $\alpha = 1/2$ would be effective for heat intensive applications. This result is further supported by [30] who showed that the largest rates of heat transfer from two downstream heat sinks in a numerically simulated two-dimensional channel flow occurred for rectangular vortex promoters with unit aspect ratio in comparison to circular and hexagonal geometries. By varying a rectangular vortex promoter through incidence angles $-45^\circ \leqslant \gamma \leqslant 45^\circ$ with a blockage ratio $\beta = 1/3$, [29] showed potential heat transfer improvements greater than 50% could be achieved. It is therefore expected that there is some finite gap height ratio and incidence angle that maximises heat transfer efficiency for quasi-two-dimensional MHD duct flow.

For ducted flows, the pressure drop in a channel is caused by viscous dissipation of energy due to internal shearing within the fluid and/or with solid boundaries [31]. Increased vorticity magnitudes, which are characterised by a decrease in scale, are less beneficial to heat transport due to an increase in internal shearing. In addition, for electrically insulated ducts it has been found, both experimentally and numerically, that the total duct pressure drop has a linear relationship with Hartmann number. For electrically conducting duct walls this relationship becomes exponential [32–34].

Research on the dependence of heat transfer and mechanical losses on Reynolds number for obstacles placed in confined MHD flows has been covered extensively [20,22–24,35–37]. In this study we restrict our investigation to *Re* = 2000 as our main consideration is developing an understanding of MHD fluid- and thermo-dynamic relations with respect to obstacle geometries. A Hartmann number of *Ha* = 200 is also considered which is double that used in comparative Q2D channel flow studies [22,23]. This is due to the continued emergence of research that has shown that the Q2D flow model may require significantly higher *Ha* values to develop [7,10,11]. It has been shown that the blockage ratio and magnetic field tend to delay the onset of unsteady flow to higher *Re* in comparison to hydrodynamic flow cases [38]. Based on the results from [22,23], a blockage ratio $\beta = 1/4$ has been adopted in the present study, as it has been shown to provide significant thermal benefits while still exhibiting unsteady flow behaviour. This is of particular importance as the present work aims to analyse the flow dynamics and heat transfer characteristics for varying gap height. If the flow were to be heavily influenced by vortex suppression due to larger blockage ratios, this could lead to difficulties in isolating a clear understanding of the thermal- and fluid- dynamics. It should also be noted that for certain orientations, natural convection may be a dominant form of heat transfer under limited conditions [38,39]. These effects are not considered in the present investigation. Furthermore, the inclusion of terms characterising the effects of viscous dissipation and Joule heating may be neglected on order of magnitude grounds for the target applications [40].

Although many studies have focused on optimising vortex promoter geometry, orientation and relative position for heat transfer enhancement in hydrodynamic channel flows, significantly less attention has been paid to the corresponding MHD duct heat transfer problem. The present work aims to identify the optimal heat transfer efficiency configurations by varying gap height and incidence angle of rectangular vortex generators with $\alpha = 1/2$ and $\beta = 1/4$ in quasi-two-dimensional MHD duct flow for *Re* = 2000 and *Ha* = 200. Additional consideration will also be given to the dependence of heat transfer and flow characteristics for $100 \leqslant Ha \leqslant 2000$.

The paper is organised as follows. The problem is defined in Section 2, which also presents the governing equations and parameters. The numerical methodology is presented in Section 3, which describes the numerical method, model setup, and validation. Results and discussion follow in Section 4, with concluding remarks and applications for this work outlined in Section 5. The final conclusions are drawn in Section 6.

2. Problem definition

The system under consideration is shown in Fig. 1. An electrically and thermally insulated rectangular cylinder with cross-section aspect ratio $\alpha = h_c/L_c = 1/2$ and blockage ratio $\beta = L_c/h = 1/4$ orientated with its axis perpendicular to the flow direction and parallel to the magnetic field vector B is confined in a long rectangular duct of length $L_{\text{duct}} = 50L_c$ with out-of-plane depth $a = 2L_c$. The origin of a Cartesian coordinate system with x and y denoting the horizontal streamwise and vertical transverse directions, respectively, is positioned at the vertical centreline of the duct and horizontally in line with the cylinder centroid. The cylinder is inclined at a counter-clockwise positive angle γ from an upright orientation (where upright refers to an orientation with the major axis of the rectangular cross-section in the vertical). The electrically insulated upper and lower duct walls are kept at representative cold and hot temperatures T_o and T_w, respectively. A homogeneous magnetic field of magnitude B acts parallel to the cylinder axis. The upstream and downstream lengths in relation to the vortex promoter centroid are $L_u = 15L_c$ and $L_d = 35L_c$, respectively. The effect of gap height ratio G/L_c of a single upright cylinder ($\gamma = 0^\circ$) for $0.8 \leqslant G/L_c \leqslant 3.2$ on heat transfer efficiency is firstly considered. The influence of cylinder incidence angle γ on heat transfer efficiency at both the duct centre-line and optimal efficiency gap height is then considered for $-90^\circ \leqslant \gamma \leqslant 90^\circ$. For each of these parameter investigations, a Hartmann Number of 200 and Reynolds number of 2000 is considered to maintain consistency with practical limitations, exhibit unstable flow behaviour, and meet the validity conditions of the quasi-two-dimensional

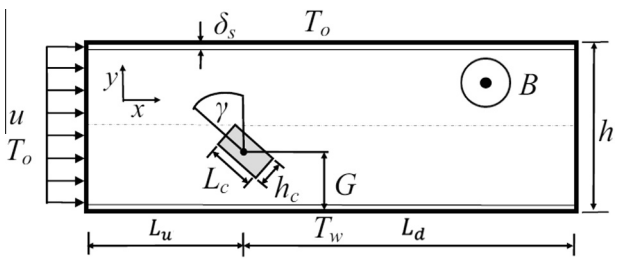

Fig. 1. Schematic diagram of the flow configuration and parameters used in the present study. Here, δ_s is the thickness of the sidewall Shercliff layers.

MHD model proposed by [1]. For completeness, the relationship between Hartmann number and heat transfer is investigated for Ha = 100, 200, 600, 1000, 1600 and 2000 at the optimal gap height ratio, in addition to a net energy balance analysis between heating power and pumping power. A Prandtl number of Pr = 0.022 was used throughout, representative of the eutectic alloy GaInSn [41].

2.1. Governing equations and parameters

Only flows with a very small magnetic Reynolds number ($Re_m \ll 1$) are considered. This renders induced magnetic fields negligible, and the magnetic field may then solely be represented by the imposed uniform transverse field [1,4]. Under sufficiently high Ha, vorticity aligns with the magnetic field, and the flow becomes quasi-two-dimensional. This study employs the quasi-two-dimensional model developed by Sommeria and Moreau [1] to describe these flows, which is referred to as the SM82 model hereafter. A detailed elaboration of the SM82 model is given by [4,15]. Here, lengths are scaled by the cylinder side length L_c, pressure by ρU_0^2 where ρ is the fluid density and U_0 is the peak inlet velocity, time by L_c/U_0, and temperature by the imposed temperature difference between the duct side-walls, ΔT. Hence, the dimensionless continuity, momentum, and energy equations can be expressed as

$$\nabla \cdot \mathbf{u} = 0, \tag{1}$$

$$\frac{\partial \mathbf{u}}{\partial t} + (\mathbf{u}\cdot\nabla)\mathbf{u} = -\nabla p + \frac{1}{Re}(\nabla^2\mathbf{u} - H\mathbf{u}), \tag{2}$$

$$\frac{\partial T}{\partial t} + (\mathbf{u}\cdot\nabla)T = \frac{1}{Pe}\nabla^2 T, \tag{3}$$

where $\mathbf{u}, p$ and T are the velocity, pressure, and temperature fields, respectively, projected onto the x–y plane. The friction parameter $H = n(L_c/a)^2 Ha = n\left(L_c^2/a\right)B\sqrt{\sigma/\rho\nu}$ represents the effect of the Lorentz force on the flow, where n represents the number of Hartmann layers formed on the duct walls (i.e. $n = 2$ for the present configuration). Here Ha, ν, σ and a are the Hartmann number, kinematic viscosity, electrical conductivity of the liquid metal, and the out-of-plane duct depth, respectively. The dimensionless parameters, Reynolds number, and Péclet number, are respectively defined as

$$Re = \frac{U_0 h}{2\nu}, \tag{4}$$

$$Pe = Re\ Pr. \tag{5}$$

The Prandtl number $Pr = \nu/\kappa$, where κ is the thermal diffusivity of the fluid.

The local Nusselt number along the heated side-wall of the channel is defined as

$$Nu_w(x,t) = \frac{h}{(T_f - T_w)}\left.\frac{\partial T}{\partial y}\right|_{\text{wall}}, \tag{6}$$

where the bulk fluid temperature, T_f, is calculated using the streamwise velocity component, u, and temperature distribution as

$$T_f(x,t) = \frac{\int_0^h uT\,\mathrm{d}y}{\int_0^h u\,\mathrm{d}y}. \tag{7}$$

The bulk fluid temperature is used here as it incorporates the mass-energy average of the temperature field within the duct. By accounting for spatial variations of mass flow and temperature, the local variations of enthalpy and heat capacity are also accounted for. This provides a clearer measure accounting for the different local heat transfer rates within the duct [42].

A time-averaged Nusselt number for heat transfer through the heated wall of the channel is calculated by first taking the time average of the local Nusselt number ($\overline{Nu}_w$) at each x-station aft of the cylinder, and then integrating over the length of downstream section of the heated side-wall using

$$Nu = \frac{1}{L_d}\int_0^{L_d} \overline{Nu}_w(x)\,\mathrm{d}x. \tag{8}$$

To measure the thermal efficiency of heat transfer augmentation, an efficiency index (also known as the augmentation Nusselt-friction-factor number) is employed. This has found widespread use in heat transfer enhancement studies using vortex generators in confined flows [23,43–45], and is given by the ratio of heat transfer enhancement to pressure drop penalty

$$\eta = \frac{HR}{PR}. \tag{9}$$

HR and PR are the heat transfer enhancement and the pressure drop penalty ratios, respectively, which are defined as

$$HR = \frac{Nu}{Nu_0}, \tag{10}$$

$$PR = \frac{\Delta p}{\Delta p_0}. \tag{11}$$

Nu and Δp are the local time-averaged bulk flow Nusselt number and total pressure drop across the duct length for the augmented cases, respectively. The subscript 0 denotes the corresponding reference values based on liquid metal flow in an obstacle free channel. The duct outer dimensions, liquid metal material properties, Reynolds number and Hartman number are identical to those used in the test cases.

2.2. Net power balance

The inclusion of a vortex promoter within the duct provides thermal enhancement but at the cost of increased pressure losses. To account for the relative importance of the two energy processes, an analytical power balance analysis is provided here, with implications for the system under investigation being discussed in Section 4.4.

The improvement in heat power due to the incorporation of the vortex promoter is

$$\Delta P_{\text{heat}} = P_{\text{heat}} - P_{0,\text{heat}}, \tag{12}$$

where P_{heat} is the heat power transferred through the heated duct wall. Here the subscript 0 again denotes the corresponding flow without cylinder, as per Section 2.1. The corresponding increase in pumping power to overcome the addition of the vortex promoter is

$$\Delta P_{\text{flow}} = P_{\text{flow}} - P_{0,\text{flow}}, \tag{13}$$

where P_{flow} is the power required to drive the flow through the duct. Hence, for net thermal improvement we require the net power balance $\Delta P_{\text{net}} = \Delta P_{\text{heat}} - \Delta P_{\text{flow}}$ to be positive.

Normalising power by $\rho L_c^2 U_0^3$ and applying the normalisations outlined in Section 2.1 for temperature, pressure, lengths and velocity, the dimensionless heat and pumping power may be expressed as

$$P_{\text{heat}} = \frac{a\kappa c_p \Delta T}{L_c^2 U_0^3}\int_{-L_u}^{L_d} \frac{\partial T}{\partial y}\mathrm{d}x \tag{14}$$

and

$$P_{\text{flow}} = 4\frac{a}{L_c}u_{\text{avg}}\Delta p, \tag{15}$$

respectively. Here c_p is the constant pressure specific heat capacity of the fluid. The changes in heat and pumping power are then

$$\Delta P_{\text{heat}} = \frac{a\kappa c_p \Delta T}{L_c^2 U_0^3} \int_{-L_u}^{L_d} \frac{\partial T}{\partial y} - \frac{\partial T_0}{\partial y} \mathrm{d}x \tag{16}$$

and

$$\Delta P_{\text{flow}} = 4\frac{a}{L_c} u_{\text{avg}}(\Delta p - \Delta p_0), \tag{17}$$

respectively. The net power balance is thus

$$\Delta P_{\text{net}} = \frac{a\kappa c_p \Delta T}{L_c^2 U_0^3} \int_{-L_u}^{L_d} \frac{\partial T}{\partial y} - \frac{\partial T_0}{\partial y} \mathrm{d}x - 4\frac{a}{L_c} u_{\text{avg}}(\Delta p - \Delta p_0). \tag{18}$$

The first term on the right hand side describes the heat flux contribution to the net balance, and the second term describes the penalty to pumping power. Pre-multiplying (18) by $L_c/4a$ allows the pre-factor to the heat flux term to be rewritten in terms of dimensionless parameters via

$$\frac{\kappa c_p \Delta T}{4 L_c U_0^3} = \frac{1}{2Pr} \frac{\nu c_p \Delta T}{2 L_c U_0^3} = \frac{1}{2PrRe} \frac{c_p \Delta T}{U_0^2} = \frac{1}{2PrReEc}. \tag{19}$$

Here the Eckert number $Ec = U_0^2/c_p\Delta T$ has been introduced, which represents the relationship between kinetic energy and enthalpy in a flow. We therefore require for net thermal enhancement that

$$\frac{1}{2PrReEc} \int_{-L_u}^{L_d} \frac{\partial T}{\partial y} - \frac{\partial T_0}{\partial y} \mathrm{d}x - u_{\text{avg}}(\Delta p - \Delta p_0) > 0. \tag{20}$$

3. Numerical methodology

A high order spectral element method was employed to discretise the governing equations. A no-slip boundary condition was applied on all solid surfaces and the channel inlet flow conditions were specified as the analytical solution for fully developed quasi-two-dimensional flow in an empty duct [4]. Imposed on the duct exit were Dirichlet and Neumann boundary conditions consisting of a constant reference pressure and a zero normal velocity gradient, respectively. A high order Neumann boundary condition is also applied on the pressure field at the other boundaries to maintain third-order time accuracy [46]. The temperature of the incoming stream and the duct upper side-wall were specified as T_o, and at the lower heated side-wall as T_w. The cylinder was thermally insulated with a zero normal temperature gradient imposed at its surface. The domain was meshed using a series of macro-elements with internally applied Langrangian polynomial mapping functions. A graded element distribution was employed towards all solid boundaries to resolve regions that experience large flow gradients, such as flow separation at cylinder corners and boundary layers.

There were an average of 4128 macro elements distributed across the domain, with small deviations away from this value of no more than $\pm 10\%$ occurring for specific configurations. The distribution of elements throughout the duct consisted of approximately 30 elements spanning its height and 139 elements (20 upstream and 119 downstream of the cylinder) spanning its length. The thermal and kinematic boundary layers were resolved with a minimum of 7 elements spanning their respective thicknesses. The present work is resolved at least as well as previous quasi-two-dimensional heat transport studies by [22,23,47].

An additional grid resolution study was conducted to ensure adequate spatial and temporal sampling to accurately resolve the dynamics of the flow field. Both local mesh refinement and element polynomial degree refinement were employed to measure the convergence of the domain size and resolution sensitive heat flux ϕ, pressure and viscous drag coefficient components $C_{d,p}$ and $C_{d,v}$, lift coefficient C_l, and $\mathcal{L}^2$ norm (the integral of velocity magnitude over the flow domain). The grid resolution study was conducted by refining the order of the elemental polynomial mapping function over $4 \leqslant N_p \leqslant 9$. The $\gamma = 0^\circ$ and $\gamma = 30^\circ$ cases were investigated to represent the extremes of expected flow complexity. Physical irregularities in the shedding of vortices led to asymmetry in advection of the wake vortices downstream. Although a general trend of convergence was obtained, the asymmetry in vortex streets led to non-monotonic convergence over the polynomial range tested. However, for the chosen polynomial order of $N_p = 8$, a convergence of better than 0.3% for all representative parameters was obtained, and this resolution is used hereafter.

Additional convergence analysis was conducted on the post processing methods used to obtain the Nusselt number and pressure drop data sets. This led to the refinement of data acquisition points and sampling frequency to accurately calculate the time history of local Nusselt number and pressure drop without significant errors or aliasing. A sampling frequency of 100 samples per unit time was used across all simulations, along with 300 sampling nodes per unit area. In the Nu and η thermal response plots in Figs. 2, 4, 6 and 10, the shaded regions about the mean trend lines represent the range between the measured global maximum and minimum responses for a given configuration. The additional error bars in these plots illustrate the uncertainty in the thermal response due to long time scale secular variations that may not be fully captured within the recorded time history. This error was estimated by calculating the relative error between the full time series and half of the time series.

The Fisher–Pearson (third moment) coefficient of skewness (ψ) statistic is employed [51] to quantify the asymmetry of the pressure and thermal data distributions across the ranges of cylinder position or incidence angle. For gap height variation and incidence angle variation cases, the central locations are $G/L_c = 0$ and $\gamma = 0^\circ$, respectively. If $\psi = 0$ the data is perfectly symmetric, while negative values indicate left skewness, and positive values right skewness.

4. Results and discussion

4.1. Gap height variation

The effect of gap height variation for an upright cylinder with $Ha = 200$ and $Re = 2000$ on the time-averaged Nusselt number, total pressure drop penalty, and corresponding overall efficiency are illustrated in Fig. 2(a)–(c), respectively. A peak in both pure heat transfer and thermal efficiency of approximately $\eta = 1.6$ occurs when $G/L_c = 1.5$, with a monotonic decrease occurring as the obstacle approaches either the upper or lower walls. The size of vortices shed from the cylinder is observed to be of order L_c. For distances $G/L_c < 1$, and approaching the lower heated wall, these vortices are increasingly suppressed by interaction with the lower Shercliff layer. Less heat is able to be transported from the lower wall and a rapid decline in $Nu, \Delta p$ and η is found. This is most readily seen in the vorticity and temperature contour plots in Fig. 3 (a). For $1 \leqslant G/L_c \leqslant 2.5$, the counter-rotating vortices are still able to interact efficiently with the lower wall thermal boundary layer; leading to the transport of large amounts of hot fluid away from the wall above the reference case level. The peak efficiency at $G/L_c = 1.5$ is driven by the outer radius of the vortical structures being at a near maximum when interacting with the heated-wall bound fluid. For distances $G/L_c > 1.5$ the vortices are shed increasingly too far from the lower wall to efficiently entrain the thermal boundary layer. Thus, a decrease in thermal enhancement is observed below the peak. The steep decline in $Nu, \Delta p$ and η for

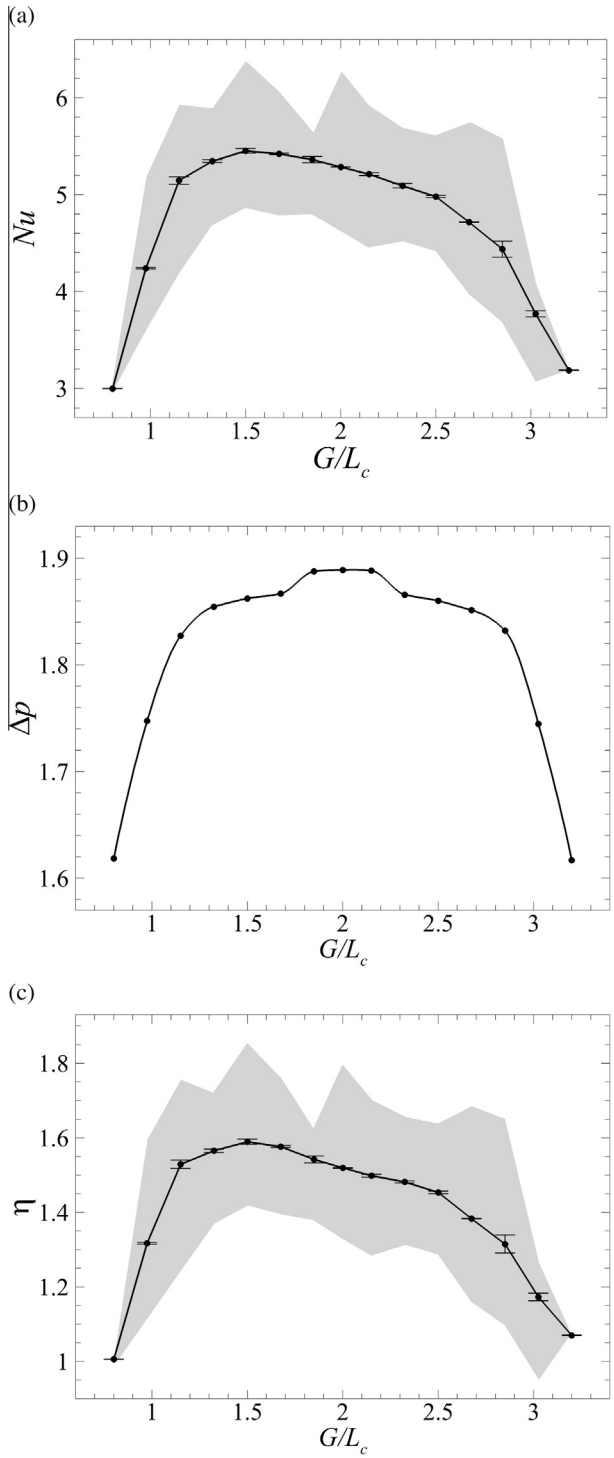

Fig. 2. Variation of (a) Nu, (b) Δp and (c) η for $Re = 2000$, $Ha = 200$ and $0.8 \leqslant G/L_c \leqslant 3.2$. The shaded regions on (a) and (c) illustrate the envelope of the secular variations of the heat transfer due to wake asymmetries. The errors bars provide an uncertainty estimate in the thermal response due to the time interval used to capture these low frequency temporal variations.

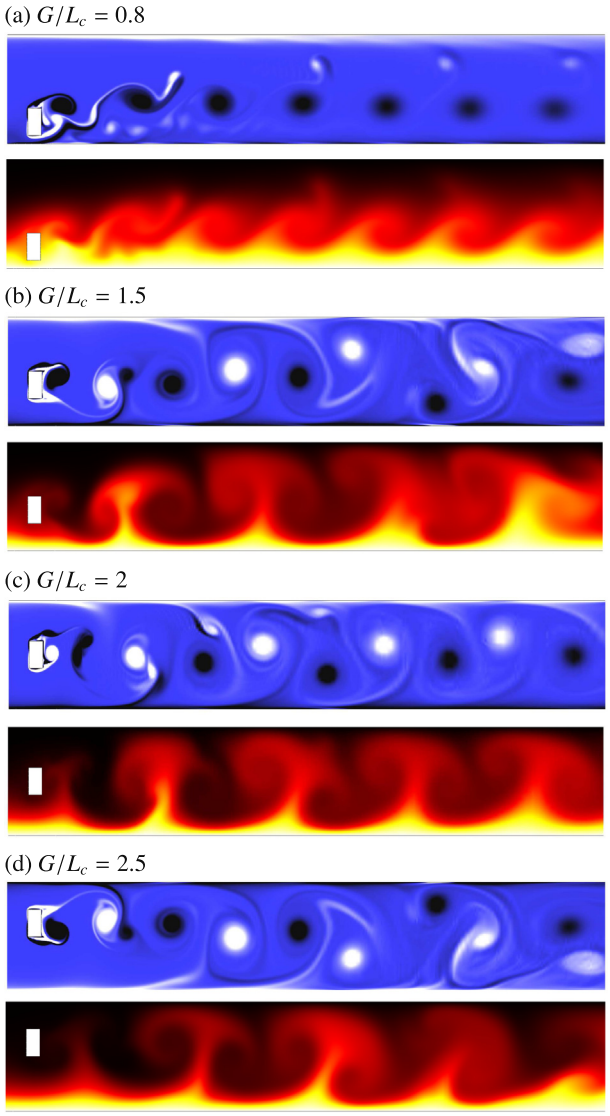

Fig. 3. Close-up (40% of the total domain) vorticity (above) and scalar temperature (below) contours for $Re = 2000$ and $Ha = 200$ for gap height ratios (a–d) of $G/L_c = 0.8, 1.5, 2$, and 2.5, respectively. The vorticity contours range is limited to approximately 10% of the minimum and maximum magnitudes observed. Darker and lighter contours represent positive clockwise rotating and negative counter-clockwise rotating vortices, respectively. The scalar temperature field contours are plotted over a range of $T_o \leqslant T \leqslant T_w$ with darker and lighter contours representing colder and hotter fluid, respectively.

$G/L_c > 2.675$ corresponds to impeding of vortices due to the influence of the upper wall. Increases in thermal enhancement and efficiency over the duct centred configuration ($G/L_c = 2$) is only found for $1.15 \leqslant G/L_c < 2$. However, all gap heights showed improved thermal efficiency over the obstacle free reference case. These findings support those discussed in the introduction with respect to a critical gap height at which heat transfer enhancement can be optimised without detrimental increases in pressure losses above the empty channel reference value of $\Delta p_0 = 1.25$ [22,23].

The localised region of increased Δp above the general trend shown in Fig. 2(b) for $1.85 \leqslant G/L_c \leqslant 2.15$ is due to the development of wake symmetry which causes the vortices to be advected downstream parallel to the duct walls. As to be expected due to the omission of natural convection and viscous heating effects in our model, the pressure drop distribution exhibits a high degree of symmetry about $G/L_c = 2$. Applying the third moment skewness coefficient to the data produces a value $\psi = 0.0073$, very close to zero skewness. In contrast, the heat transfer response demonstrates a significant negative skewness of $\psi = -0.437$, indicating a strong bias towards smaller gap heights for increased thermal enhancement. The combination of a reduction in pressure losses and the increase in thermal boundary layer entrainment for $1.15 \leqslant G/L_c \leqslant 2$, leads to the observed increase in thermal efficiency for these cylinder positions, as shown in Fig. 2(c).

For the centred case shown in Fig. 3(c), periodic shedding of opposite-signed vortices from the cylinder shear layers are observed, leading to the formation of a Kármán vortex street. At this blockage ratio $\beta = 1/4$, the interaction of this vortex street with the Shercliff layers leads to a substantial loss of wake coherence. This behaviour is amplified when the cylinder is moved closer to either duct wall, where the vortex wake also decays more rapidly downstream. These findings are consistent with those found in [23] for circular cylinders at $\beta = 0.3$ and $\beta = 0.2$, and confirmed by the breakdown of the two-dimensional Kármán vortex street shown by [14,38]. As illustrated in Fig. 2(b), mechanical pressure losses also decline rapidly for distances approaching both duct walls as vortex suppression leads to a significant reduction in viscous shear stress.

The shaded region about the mean trend line depicted in Fig. 2 (a) and (c) illustrate the very low frequency variations of these quantities over time. The size of the shaded region is influenced by the degree of time-dependent asymmetry of the wake and the breakdown of the vortex street due to interaction with the Shercliff layers; both of which tend to causes a loss of periodicity and coherence in the thermal structures. Higher degrees of influence causes the thermal response to become more disordered and the magnitude of variations tend to increase. Points exhibiting a smaller shaded region are closer to time periodicity. The wake asymmetry and breakdown of the vortex street is highlighted by the vorticity contour plots for $G/L_c = 1.5, 2$ and 2.5 in Fig. 3(b)–(d). It was also observed that wake asymmetry leads to a time-dependent lateral oscillation of the vortex street as it convects downstream. The wake continually shifts between states in which vortices are advected towards either the interior of the duct or parallel to the duct walls downstream. These results are consistent with observed phenomena in previous studies of impeded MHD flows for similar interaction parameters and blockage ratios [6,18]. It has been suggested that the causes of this asymmetry in vortex wakes may be due to slight differences in the shedding frequency of vortices from the cylinder separation points [18]. At height ratios where there is large suppression of near wall vortices, such as $G/L_c = 0.8$, the variation in thermal response becomes dominated by the periodic shedding of vortices from the cylinder's upper surface, which is highlighted by the smaller shaded regions around these data points. The error bars presented in Fig. 2(a) and (c) remain relatively small for all measured data sets. This implies that the low frequency variations of the thermal response is sufficiently captured in the time intervals used for integration.

4.2. Incidence angle variation

4.2.1. $G/L_c = 2$

The effect of varying the cylinder incidence angle over $-90^\circ \leqslant \gamma \leqslant 90^\circ$ for a duct-centred cylinder with $Ha = 200$ and $Re = 2000$ on the time-averaged Nusselt number, total pressure loss penalty and the overall efficiency are illustrated in Fig. 4(a)–(c), respectively. Interestingly, there is no significant increase in thermal enhancement through cylinder inclination in comparison to an upright cylinder at the same gap height. However, due to the combination of a global reduction in pressure loss penalties and a local region of increased heat transfer, efficiency is maximised at $\eta = 1.58$ for an incidence angle of $\gamma = -37.5^\circ$. These results raise an important point with respect to the aim of this research. Namely, the best performing configuration from an efficiency standpoint is not necessarily the one with the largest heat transfer enhancement if it incurs substantial mechanical losses. Local sharp changes away from the general thermal enhancement trend, such as for $-45^\circ < \gamma \leqslant 0^\circ$, tend to suggest that the wake dynamics and in turn the thermal response are highly sensitive to the coupling of shedding frequency and distance between the cylinder separation points. Increases in thermal efficiency over an upright cylinder are also found for $\gamma = -7.5^\circ$ and $0^\circ < \gamma \leqslant 22.5^\circ$. This response is driven by the larger negative rates of change for Δp in comparison to Nu for the incidence angles in this region. It should however be noted that all of the measured thermal efficiency indices are less than the optimal gap height variation case of $\eta = 1.6$ at $G/L_c = 1.5$ and $\gamma = 0^\circ$.

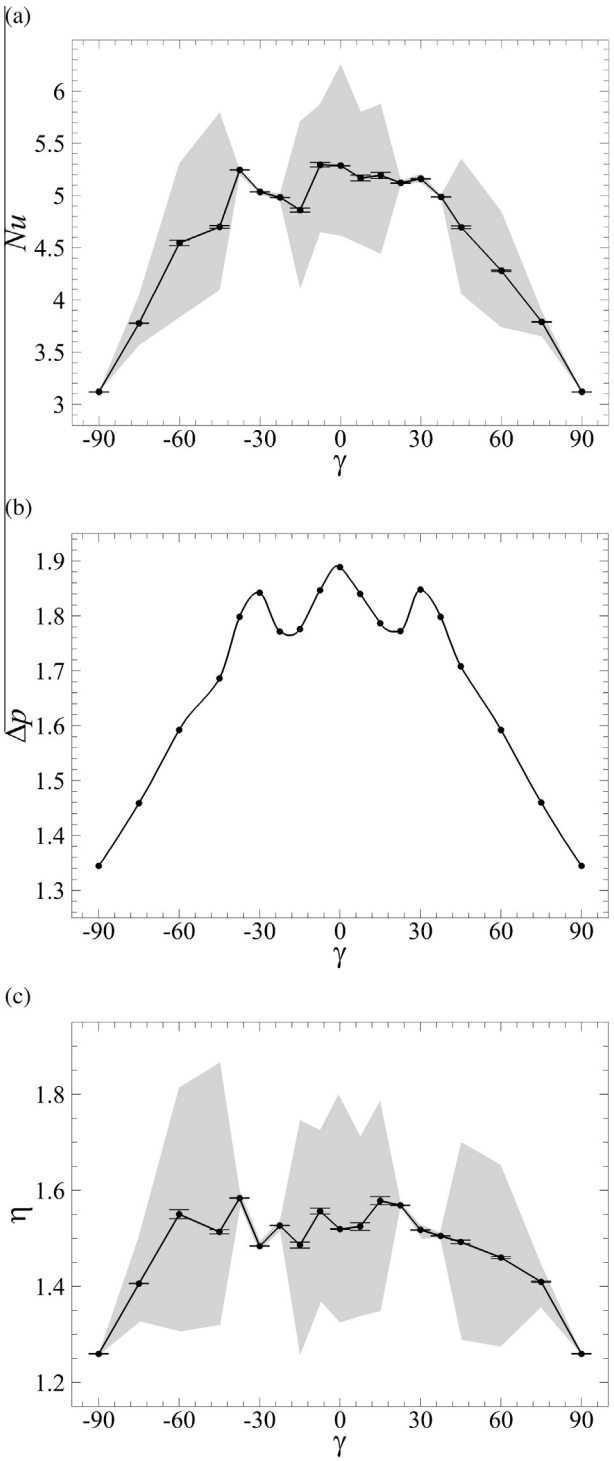

Fig. 4. Variation of (a) Nu, (b) Δp and (c) η for $Re = 2000$, $Ha = 200$, $G/L_c = 2$ and $-90^\circ \leqslant \gamma \leqslant 90^\circ$. The shaded regions and error bars on (a) and (c) are per Fig. 2.

A monotonic decrease of Nu and Δp is observed for $|\gamma| > 37.5^\circ$ to minima at $|\gamma| = 90^\circ$. As to be expected based on the symmetry of the geometry at this cylinder position, the pressure drop

distribution exhibits a high degree of symmetry about $\gamma = 0^\circ$ indicated by a skewness coefficient of $\psi = 0.009$. The thermal response shows a skewness coefficient of $\psi = 0.0195$, illustrating a slight bias towards positive incidence angles for increased heat transfer.

From $|\gamma| = 0^\circ$ to 22.5°, Δp decreases before slightly increasing again to $|\gamma| = 30^\circ$, then subsequently decreasing rapidly for $|\gamma| > 30^\circ$. Visualisation of instantaneous vorticity and temperature fields for several of the cases from Fig. 4 are shown in Fig. 5. As highlighted by Fig. 5(c), interaction between lower wall and cylinder shear layers causes the wake to be advected downstream parallel to the out-of-plane duct walls for $\gamma = 22.5^\circ$. This behaviour is consistent for other angles in these regions and has the effect of reducing viscous dissipation, and thus leading to the decline in Δp observed for $0^\circ \leqslant |\gamma| \leqslant 22.5^\circ$.

For the $\gamma = -37.5^\circ$ case shown in Fig. 5(b), we see the outer regions of the vortices shed from the cylinder's lower separation point merging effectively with the lower wall thermal boundary layer, and in turn leading to the observed peak in η. Wake coherence downstream is maintained at this incidence angle, leading to the creation of consistent broad plumes of hot temperature fluid being transported away from the lower wall.

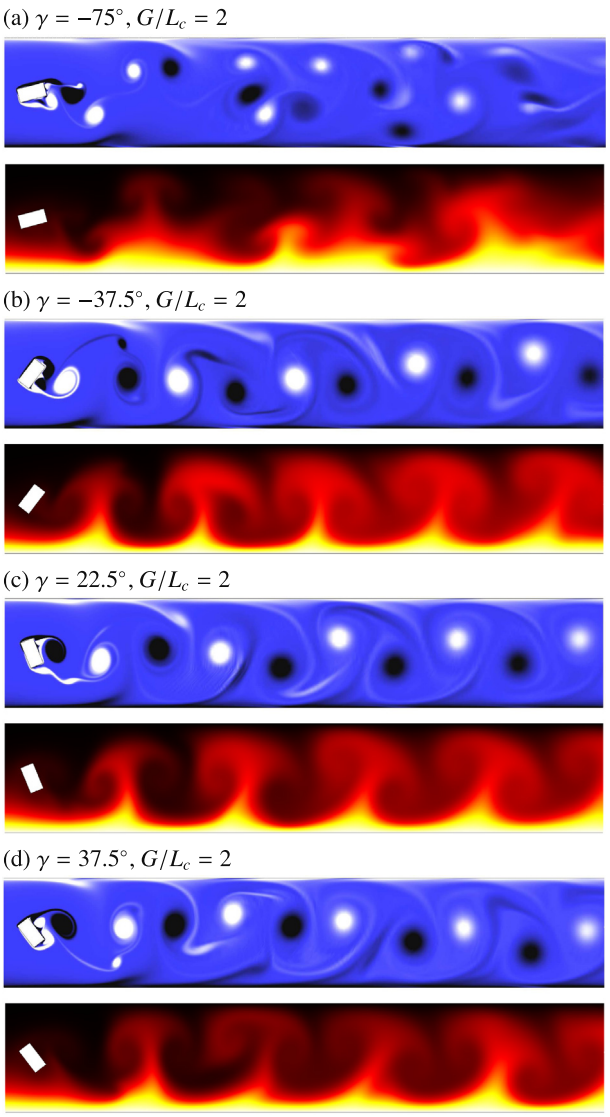

Fig. 5. Close up (40% of the total domain) vorticity (above) and scalar temperature (below) contours for $Re = 2000$, $Ha = 200$ and $G/L_c = 2$ for incidence angles (a–d) of $\gamma = -75^\circ, -37.5^\circ, 22.5^\circ, 37.5^\circ$, respectively. The contour colour map and range are per Fig. 3.

Cylinder inclination also leads to a reduction in wake thickness and effective blockage ratio. These effects combine to cause a reduction in thermal enhancement from decreased wake size, and a decline in pressure losses by reducing cylinder drag forces caused by surface pressure differentials and viscous shearing in the wake. With respect to heat transfer enhancement, for angles approaching $|\gamma| = 90^\circ$, co-rotating vortices are formed due to suppression of vortices shed from either the lower or upper cylinder shear layers. Hence, regions between the vortices do no exhibit strong upward thermal plumes (as shown in Fig. 5(a)) in comparison to full wakes with coherent counter-rotating vortical structures (such as Fig. 5 (b)–(d)).

As highlighted by the shaded regions on Fig. 4(a) and (c), angles in the region $22.5^\circ \leqslant |\gamma| \leqslant 37.5^\circ$ show small secular variations of Nu over time. In this region, the heat transfer enhancement response is in lock-step with the periodic shedding of the vortices. For these incidence angles, the thermal response is not heavily affected by lateral wake oscillations or the loss of wake coherence caused by interactions with the Shercliff layers. This is nicely illustrated by the clear periodic plumes of hot fluid carried downstream coinciding with the advection of the vortex structures shown in Fig. 5(b)–(d).

As shown through a comparison of Fig. 5(c) and (d), the width of the vortex wake expands with increasing angle magnitude for $0^\circ \leqslant |\gamma| \leqslant 30^\circ$, then proceeds to decrease for $|\gamma| > 30^\circ$. This is caused by the symmetry of the top and bottom cylinder corners traversing the maximum duct height distance at $|\gamma| < 26.56^\circ$. For $37.5^\circ \leqslant |\gamma| \leqslant 75^\circ$ the opposite-signed vortices shed from the cylinder's trailing and leading edges merge aft of the obstacle; resulting in a large reduction in circulation. The coherence of the Kármán vortex street is increasingly lost, and the wake decays rapidly downstream. The extreme of this behaviour is most readily seen in vorticity and temperature contour plots for $\gamma = -75^\circ$ in Fig. 5 (a). For negative incidence angles, the merging of the leading and trailing edge shear layers lead to displacement of the wake towards the lower heated wall. The opposite behaviour is seen for positive incidence angles, where the vortices are advected upwards towards the upper wall. Again, the very low frequency variations of the thermal response is sufficiently captured in the time intervals used for integration. Hence, the error bars presented in Fig. 4(a) and (c) remain relatively small for all measured data sets.

4.2.2. $G/L_c = 1.5$

The effect of incidence angle for $-90^\circ \leqslant \gamma \leqslant 90^\circ$ for a cylinder offset from the duct centre-line at $G/L_c = 1.5$ with $Ha = 200$ and $Re = 2000$ on the time-averaged Nusselt number, total pressure drop and the corresponding overall efficiency are illustrated in Fig. 6(a)–(c), respectively. Consistent with the duct-centred case, improvements in thermal efficiency can be achieved through cylinder inclination. A peak of $\eta = 1.7$ was achieved at $\gamma = -37.5^\circ$, which corresponds to an approximate 12% increase over an upright cylinder. Increases in thermal efficiency were also achieved in the regions $-37.5^\circ < \gamma \leqslant 22.5^\circ, -7.5^\circ \leqslant \gamma < 0^\circ$ and $0^\circ < \gamma \leqslant 15^\circ$. In comparison to the trends observed for the centred case, pure heat transport was improved over the upright cylinder for incidence angles of $\gamma = -37.5^\circ$ and 7.5° at this gap height.

A monotonic decrease in Nu and Δp is again observed for $|\gamma| > 37.5^\circ$ to minima at $|\gamma| = 90^\circ$. However, a minimum thermal efficiency is now obtained at $\gamma = -75^\circ$ due to a reduction in the rates of change of heat transfer in this region. In comparison to the pressure distribution shown in Fig. 4 for the centred case, the pressure distribution shown in Fig. 6(b) experiences a higher degree of asymmetry about the $\gamma = 0^\circ$ orientation, with a skewness coefficient of $\psi = -0.144$. This indicates that greater pressure losses are generally found for negative incidence angles. The thermal response exhibits a slight skewing towards negative incidence

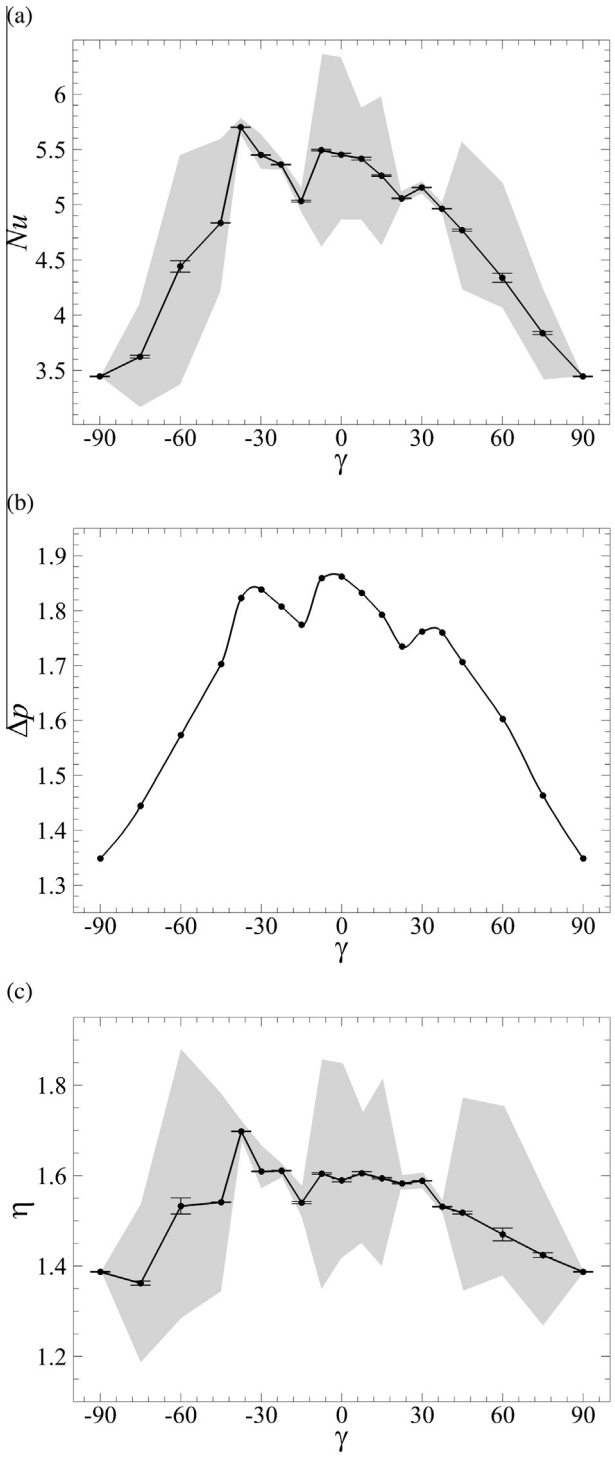

Fig. 6. Variation of (a) Nu, (b) Δp and (c) η for $Re = 2000$, $Ha = 200$, $G/L_c = 1.5$ and $-90^\circ \leqslant \gamma \leqslant 90^\circ$. The shaded regions and error bars on (a) and (c) are per Fig. 2.

angles for heat transfer enhancement with $\psi = -0.068$. Localised regions of decreased mechanical losses are again seen for $-15^\circ \leqslant \gamma \leqslant -7.5^\circ$ and $0^\circ \leqslant \gamma \leqslant 22.5^\circ$ for similar reasons to those discussed in Section 4.2.1. Time periodicity of the thermal response is again recovered in the regions $22.5^\circ \leqslant |\gamma| \leqslant 37.5^\circ$ which are driven predominantly by the shedding frequency of the vortices. Hence, the extent of the secular variations of the thermal response, and in turn the size of the shaded regions on Fig. 6(a) and (c) are observed to be at a minimum. To help quantify this behaviour, Fig. 7 presents the scaled mean Fourier spectra for the time-dependent Nusselt number for both the $\gamma = -37.5^\circ$ and $\gamma = 0^\circ$ cases. Consistent with the $\gamma = -37.5^\circ$ uniform vorticity and scalar structures seen in Fig. 8(b), the corresponding Fourier spectrum exhibits strong narrow peaks and harmonics corresponding to the highly periodic and uniform heat transfer response. In contrast, the $\gamma = 0^\circ$ case shows a significant increase in spectrum energy as $\omega \to 0$, coupled with a considerable widening of the peaks and dispersion of energy across the spectrum. This is consistent with the comparable increase in wake disorder and loss of coherent thermal boundary layer entrainment seen in the vorticity and temperature contour plots in Fig. 8(b). The increased wake disorder and loss of periodicity of the thermal response for the $\gamma = 0^\circ$ tends to increase

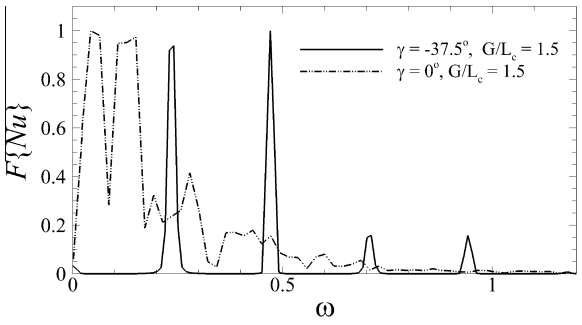

Fig. 7. Fourier spectra of the time-dependent Nusselt number ($F\{Nu\}$) for $\gamma = 0^\circ$ and -37.5° at $G/L_c = 1.5$, $Ha = 200$ and $Re = 2000$.

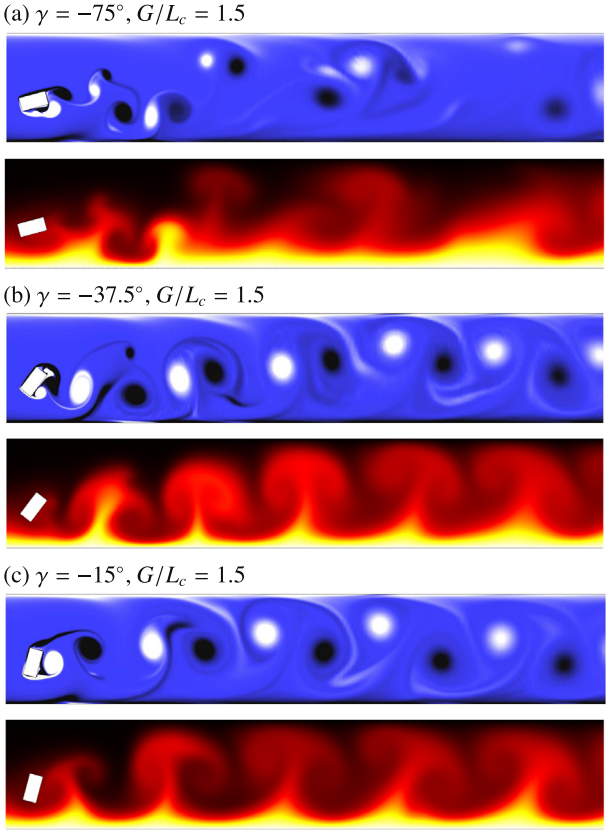

Fig. 8. Close-up (40% of the total domain) vorticity (above) and scalar temperature (below) contours for $Re = 2000$, $Ha = 200$ and $G/L_c = 1.5$ for incidence angles (a–c) of $\gamma = -75^\circ, -37.5^\circ, -15^\circ$, respectively. The contour colour map and range as per Fig. 3.

the variation of heat transfer over time. This is highlighted by the large differences in the size of the shaded region around incidence angles $\gamma = 0^\circ$ and $\gamma = -37.5^\circ$ shown in Fig. 6(a) and (c).

As illustrated via the vorticity and temperature contours in Fig. 8(c), the localised decrease in the general *Nu* trend around $\gamma = -15^\circ$ is due to the shearing of the vortex pair towards the upper wall immediately after forming. For this case, the wake does not interact strongly with the lower wall until further downstream, where much of the angular momentum transporting hot fluid upwards has already been dissipated. For the peak efficiency case, shown in Fig. 8(b), the opposite behaviour is now observed. The vortex pair is advected downward towards the lower wall while the angular momentum is at a near maximum; thus, effectively sweeping hot fluid away from the lower wall at increased rates. Furthermore, the vortices are shed at such an angle as to maximise the interaction time with the lower wall thermal boundary layer as they are advected downstream.

In contrast to the duct-centred cylinder, the direction that the vortices are advected tends to be more heavily influenced by the interaction with the lower Shercliff layer than the distance between the cylinder separation points. However, as highlighted in Fig. 8(a), for $37.5^\circ \leqslant |\gamma| \leqslant 75^\circ$, we again see that the merging of the vortex pair aft of the obstacle leads to a large reduction in vorticity. This in turn leads to a chaotic disordered wake which is detrimental to heat transport within the channel. The relatively small error estimates shown in Fig. 2(a) and (c) suggest that the low frequency variations of the thermal response are sufficiently captured in the time intervals used for integration.

4.3. Streamwise distribution of local Nusselt number

The time-averaged local Nusselt number distribution as a function of streamwise direction aft of the cylinder (x_d) is now considered for a selection of illustrative cases at $G/L_c = 1.5$. Fig. 9 presents Nu_w for the $\gamma = -37.5^\circ, -7.5^\circ, 0^\circ$ and 45° cases at $Re = 2000$ and $Ha = 200$. Localised peaks and troughs correspond to streamwise locations where the mean wake path is cast closest to and furthest from the heated lower wall, respectively. For the global peak efficiency case at $\gamma = -37.5^\circ$, distribution of *Nu* remains relatively constant downstream. The mean flow of the wake follows a consistent path without significant time-dependent oscillations. This behaviour is consistent for all of the time-periodic thermal responses as highlighted in the preceding sections. However, due to the maintenance of wake coherence for this configuration, heat transfer remains relatively high along the whole duct length. Due to the symmetry of the fixed separation points at $\gamma = 0^\circ$, the upright cylinder experiences a steady decline in Nu_w downstream. The thermal response is driven by the dissipation of vorticity downstream rather than a loss of wake coherence or time-dependent lateral oscillations.

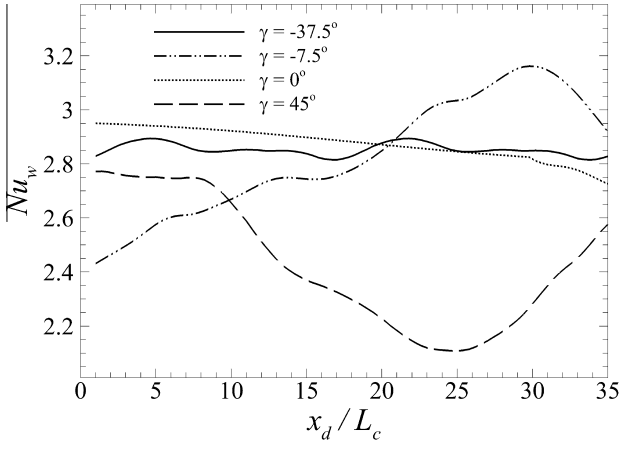

Fig. 9. The local time-averaged Nusselt number for $Re = 2000$, $Ha = 200$, $G/L_c = 1.5$ and $\gamma = -37.5^\circ, -7.5^\circ, 0^\circ$ and 45° plotted against the scaled streamwise direction. Here $x_d/L_c = 0$ corresponds to the cylinder centroid position. Measurements are taken for $1 \leqslant x_d/L_c \leqslant 35$ to allow for changes in effective length as the cylinder incidence angle is varied.

For incidence angles where the thermal response is significantly irregular over time, downstream locations are subjected to greater variation in the rates of heat transport. For negative incidence angles, the time-averaged mean flow increases the rate of heat transport to a peak further downstream. For the $\gamma = -7.5^\circ$ case shown in Fig. 9, this peak occurs at approximately $x_d = 30L_c$ before proceeding to decrease downstream. In contrast, for positive incidence angles, we see a decline in the time-averaged Nusselt number to a minimum further downstream. For the $\gamma = 45^\circ$ case shown in Fig. 9, this occurs at approximately $x_d = 25L_c$ before subsequently increasing again for larger x_d. The location of the global streamwise peak and trough of the local Nusselt number are a direct function of the obstacle incidence angle, the distance between the fixed separation points and the *Re* and *Ha* dependent vortex shedding frequency. These time-averaged regions of increased and decreased local heat transport suggest that the previously measured irregularity in the thermal response is dominated by the loss of clear vortical structure and wake coherence, rather than time-dependent lateral oscillations.

4.4. Net energy analysis

The form of the net power balance relationship given by Eq. (20) will be analysed in the present section along with its implications for magnetic confinement fusion reactor applications. The form of the pre-factor $1/PrReEc$ in Eq. (20) shows that any net benefit in heat transfer enhancement will be more significant for smaller Prandtl numbers, smaller Reynolds numbers, and smaller Eckert numbers. Liquid metal flows tend to have relatively small Prandlt numbers (the $Pr = 0.0022$ used here is representative of GaInSn eutectic alloys used in laboratory experiments, while lead–lithium alloys in fusion applications can be even lower [50]), indicating that thermal diffusivity is orders of magnitude larger than molecular diffusivity. Current fusion cooling blanket designs also tend to involve relatively modest Reynolds numbers of order $O(10^3) - O(10^4)$. Furthermore, representative Eckert numbers tend to be of order $O(10^{-9})$, indicating that enthalpy in the flow is substantially higher than kinetic energy [48]. For fusion applications the pre-factor is therefore very large ($\gg 1$), strongly amplifying the benefit due to heat transfer enhancement in comparison to elevation in required pumping power.

To illustrate this point further, representative values for common magnetic fusion reactor applications will be analysed. Dual-Coolant Lithium Lead (DCLL) type blankets are a primary candidate for the DEMO fusion reactor design [48], and the ITER nuclear fusion research and engineering project will test Helium-Cooled Lithium–Lead (HCLL) Tritium Breeding Blankets (TBBs); both of which will employ 90% ^{6}Li in lithium eutectic alloy Pb–15.7Li. The properties of Pb–Li alloys are aggregated in [49]. Formulas for estimating κ and c_p using these properties are taken from [50] and estimates for $\Delta T, L$ and U_0 are given in [48]. They are as follows: $\kappa \approx 9 \times 10^{-6}$ to 1.2×10^{-5} m^2/s, $c_p \approx 186$ to 188 J/kg K, $\Delta T = 250$ K (measured from the inlet and outlet fluid temperatures), $L = 0.1$ m and $U_0 = 0.015$ m/s, giving estimates of the pre-factor ranging over

$$\frac{1}{2PrReEc} = 6.2 \times 10^5 \text{ to } 8.3 \times 10^5. \tag{21}$$

Substituting these estimates into Eq. (18), along with the results for the global minimum efficiency case ($G/L_c = 0.8, \gamma = 0^\circ$) in the present study gives a dimensionless net power increase of $\Delta P_{net} \approx 1.07 \times 10^8$ to 1.43×10^8. Hence, even for the lowest performing configuration from an efficiency standpoint, the low Prandtl and Eckert numbers and modest Reynolds numbers in fusion applications dictate that significant increases in net power over the reference case can be achieved.

4.5. Hartmann number dependence

The influence of Hartmann number on the heat transfer, pressure drop, and the lift coefficient fluctuation is now considered. A configuration featuring an upright cylinder offset at $G/L_c = 1.5$ is investigated over Hartmann numbers $100 \leqslant Ha \leqslant 2000$. Fig. 10(a) shows the dependence of Nusselt number with Hartmann number at these conditions. A monotonic decrease in Nu with increasing Hartmann number is observed, and the low frequency temporal variations of the thermal response reduce for larger Ha, becoming negligible for $Ha \gtrsim 1000$. This is revealed by the narrowing of the shaded region in Fig. 10(a) with increasing Hartmann number.

In order to develop a physically meaningful relationship for this Nu–Ha data, we reason that at $Ha = 0$ the flow will exhibit a finite Nusselt number, and similarly as $Ha \to \infty$ a finite positive asymptotic Nusselt number (Nu_∞) will be approached. The first assumption is well-supported by an abundance of laboratory and theoretical work on heat transfer in hydrodynamic duct flows. The scale analysis to follow supports the second assumption. In the limit as $Ha \to \infty$ at a fixed Re, the Shercliff layer thickness $\delta_s \to 0$ as these scale as $\delta_s/a \sim Ha^{-1/2}$. Hence the transverse profile of streamwise velocity across the duct approaches $U(y) \to U_0$, and the bulk fluid temperature defined by Eq. (7) reduces to

$$T_f = \frac{1}{h}\int_0^h T\,\mathrm{d}y. \tag{22}$$

A balance between vertical diffusion of heat from the heated duct wall into the flow with the uniform streamwise transport of heat yields a scaling for the thermal boundary layer thickness as $\delta_T \sim \sqrt{x\kappa/U_0}$, where here x is taken from the upstream point of thermal layer growth. Normalising by channel height h and rewriting in terms of the control parameters defined in this study produces

$$\frac{\delta_T}{h} \sim \frac{1}{2}\sqrt{\frac{x}{h}\frac{1}{Pe}}. \tag{23}$$

It is convenient to define a relative temperature that is zero outside the thermal boundary layer and unity at the hot wall, $T' = (T - T_0)/(T_w - T_0)$, with T_0 the cold upstream fluid temperature. This renders the integrand in Eq. (22) non-zero only within the thermal layer, giving

$$T_f = T_0 + \frac{1}{h}(T_w - T_0)\int_0^{\delta_T} T'\,\mathrm{d}y. \tag{24}$$

Substituting into Eq. (6) yields

$$Nu_w = \frac{h}{\frac{1}{h}(T_w - T_0)\int_0^{\delta_T} T'\,\mathrm{d}y - (T_w - T_0)\left.\frac{\partial T}{\partial y}\right|_{\text{wall}}}. \tag{25}$$

Consideration of the orders of magnitude of quantities within the thermal layer reveals $O(\partial T/\partial y) \approx (T_w - T_0)/\delta_T$ and $O\left(\int_0^{\delta_T} T - T_0\,\mathrm{d}y\right) \approx \frac{1}{2}(T_w - T_0)\delta_T$. Substituting these into Eq. (25) yields

$$O(Nu_w) \approx \frac{1}{\delta_T/h - \frac{1}{2}(\delta_T/h)^2}, \tag{26}$$

which for thermal layer thicknesses much less than the channel height, $\delta_T/h \ll 1$, simplifies to

$$Nu_w \sim \frac{h}{\delta_T} \sim 2\sqrt{Pe\frac{h}{x}}. \tag{27}$$

Hence a finite asymptotic value of Nu is expected in the limit as $Ha \to \infty$ which scales as $Nu \sim Pe^{1/2}$.

Several alternative curve functions satisfying the requirements of monotinicity, finite Nu at $Ha = 0$ and finite asymptotic Nu as $Ha \to \infty$, were investigated. An optimisation study was performed on each relationship to determine the coefficients maximising the correlation coefficient r^2. The best fit obtained was $Nu = 3.244\exp(-0.001Ha) + 2.875$, which is plotted in Fig. 10(a), achieving a correlation coefficient of $r^2 = 0.9995$. This relationship predicts for this configuration at a fixed Re an estimated $Nu = 6.12$ at $Ha = 0$ and an asymptotic $Nu_\infty \to 2.875$ as $Ha \to \infty$. It is interesting to see in this expression that $Nu - Nu_\infty$ is exponentially damped with a decay rate proportional to Hartmann number similarly to the quasi-two-dimensional Hartmann braking term in the momentum.

Owing to the electrically insulating duct walls, the total duct pressure drop follows a perfectly linear relationship with Hartmann number, as shown in Fig. 10(b). This result is consistent with the experimental and numerical studies presented in the

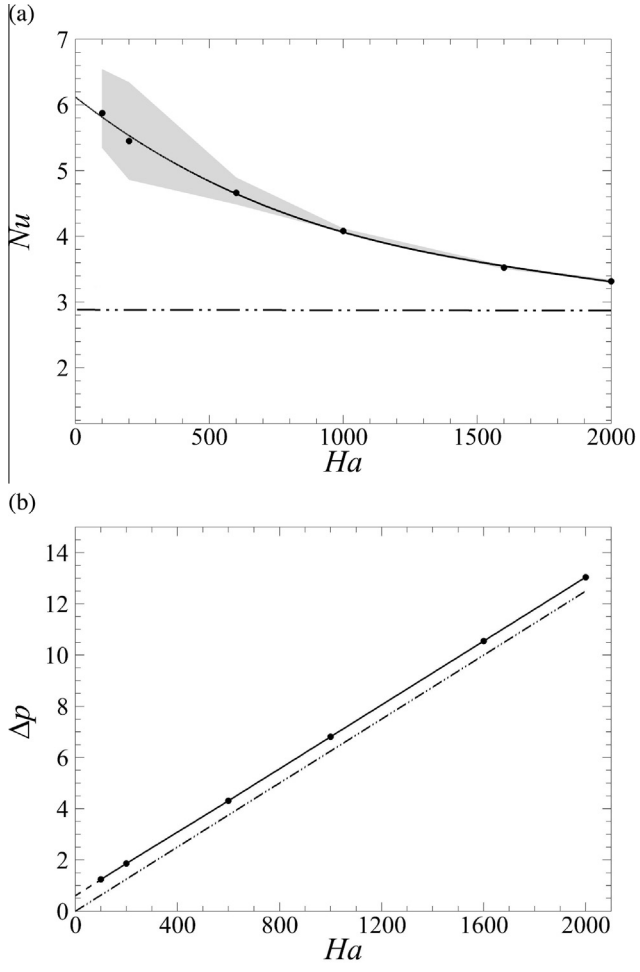

Fig. 10. Variation of (a) Nu and (b) Δp for $100 \leqslant Ha \leqslant 2000$, $Re = 2000$, $G/L_c = 1.5$ and $\gamma = 0^\circ$. The shaded regions and error bars on (a) are per Fig. 2. The dash-dotted line on (a) is the asymptotic Nu as $Ha \to \infty$. The dashed-dotted line on (b) is the analytical solution for fully developed flow in an empty channel under the SM82 model.

introduction [32,33]. The quasi-two-dimensional analytical solution for an empty channel total pressure drop can be derived using Eq. (2) by considering a stream-line through the uniform core flow region (where $\partial/\partial t = \partial/\partial x = \partial u/\partial y = v = 0$), yielding $\Delta p_0/(L/L_c) = 2(L_c/a)^2 Ha/Re$. Substituting the present $Re = 2000, L_c/a = 1/2$ and $L = 50L_c$ yields $\Delta p_0 = 0.0125Ha$, which is plotted in Fig. 10(b). The shifting of the measured obstructed-duct flow curve upwards and away from the empty-duct analytical solution highlights the influence that an obstacle has on the pressure drop response. Although the inclusion of the vortex promoter does increase the mechanical pressure losses, this adverse effect on efficiency becomes increasingly insignificant for larger *Ha* values. For moderate to high magnetic field strengths ($Ha > 100$) the mechanical penalty is driven predominantly by increased levels of frictional Hartmann dampening, rather than increased viscous dissipation due to larger flow disturbances. For the *Ha* = 100, 600 and 1000 cases, the percentage contribution of Hartmann damping to the total friction losses are 51%, 85% and 91%, respectively.

Increases in the magnitude of *Ha* leads to greater lift coefficient periodicity and improved wake coherence. However, due to the increased levels of frictional dampening, the amplitude of the lift coefficient is progressively decreased as shown in Fig. 11(a)–(d).

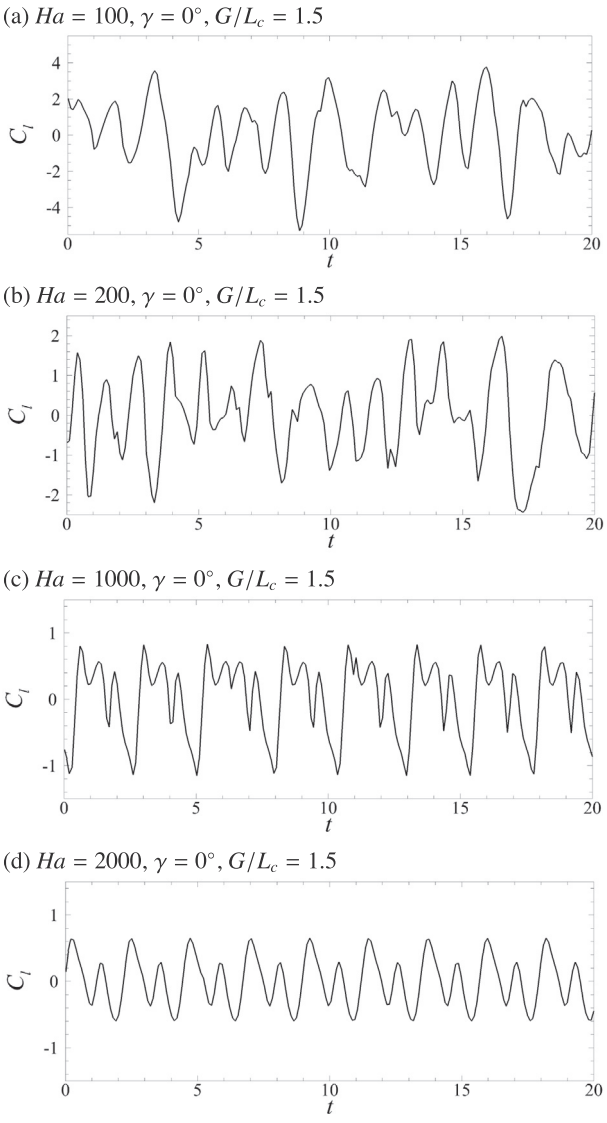

Fig. 11. Time history lift force coefficient for (a–d) *Ha* = 100, 200, 1000 and 2000, respectively. For each case $\gamma = 0°, G/L_c = 1.5$ and *Re* = 2000.

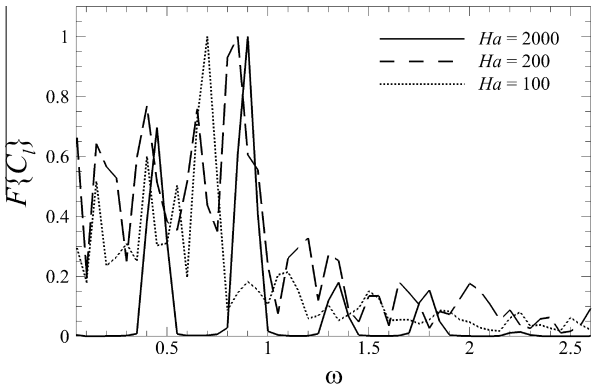

Fig. 12. Fourier spectra of the lift coefficient ($F\{C_l\}$) for *Ha* = 100, 200 and 2000 with $\gamma = 0°, G/L_c = 1.5$ and *Re* = 2000.

This amplitude reduction correlates with a decrease in the vortex scale and narrowing of the wake. Fig. 12 presents the scaled Fourier spectra of the lift coefficient for three of the representative cases presented in this section. Consistent with the lift coefficient plots in Fig. 11, an increase in the dispersion of energy across the spectrum coincides with increased irregularity in the response of C_l. Furthermore, for increasing magnetic field strength, we see a slight shift in the peak frequency to larger values, coupled with a narrowing of the fundamental, harmonic and sub-harmonic peaks. These results are also consistent with a reduction in the time-dependent variation of the thermal response for increasing *Ha* as illustrated by the shaded region on Fig. 10(a). In addition, there is also an approximately 25% increase in the shedding frequency as *Ha* increases from 100 to 2000.

5. Discussion

From a practical engineering standpoint, the introduction of a single cylinder at all but the closest distances to the heated duct side-wall can prove substantially beneficial to thermal efficiency over an empty channel in MHD duct flows; with the global minimum increase in efficiency across this investigation being 31.8%. A single rectangular cylinder inclined at $\gamma = -37.5°$ and offset at $G/L_c = 1.5$ reaching an efficiency index of $\eta = 1.7$ appears to be the most optimal configuration borne out from the results of this study. However, as shown through the analysis of the streamwise distribution of Nu_w and the dependence on *Ha*, the measured improvements can be significantly affected by the combination of shedding frequency and incidence angle. Thermal efficiency generally responded better to cylinder inclination for the offset cylinder cases. However, for both the centred and offset test cases, heat transfer efficiency was only improved over an upright cylinder in narrow localised bands of incidence angles. These isolated regions of increased thermal efficiency may be difficult to realise in a practical implementation, where greater engineering tolerances are often required, and deviations from a perfectly uniform upstream flow are likely.

Notably the maximum achievable efficiency found in the present work is comparable to the range of $1.68 \leqslant \eta \leqslant 2.05$ found by [23] for circular cylinders with blockage ratios of $\beta = 0.2$ and $\beta = 0.3$ at *Ha* = 100, respectively. As shown in previous works [20,24] and in Section 4.5, increasing *Ha* is detrimental to heat transfer, total pressure drop and in turn thermal efficiency. These results help to highlight the significance of the results borne out from this study. Namely, that the increased damping at higher *Ha* requires careful consideration of geometric parameters when trying to generate the kinds of vortex promoter wake flows required to optimally enhance heat transfer. The comparable

efficiency indices found in the present work, shows that via careful consideration of vortex promoter orientation, efficiency levels that are found in more favourable flow conditions, such as in [23], can be achieved. For applications where a great deal of importance is placed on achieving a positive net energy balance, such as magnetically confined fusion reactors, the present works significantly contributes to the understanding necessary to develop complex heat transport systems by connecting the relationships between different wake dynamics and vortex promoter orientations.

In comparison to hydrodynamic studies, the measured maximum efficiency achieved here was significantly higher than those found by [29], who experienced much larger pressure penalties for all test cases. However, regions of improved thermal enhancement produced by lowering and inclination of an obstacle were confirmed in the present work. Direct comparison between results is difficult not only due to the hydrodynamic nature of those flows, but also due to the slightly lower Reynolds number and marginally larger blockage ratio used. This larger blockage ratio is likely to be the main cause of the greater pressure losses measured. Finally, it is reiterated that the configuration producing the maximum heat transfer is often not the most efficient when comparing pumping power to heat extraction. This is especially important when one has to consider the efficiencies associated with converting thermal energy into usable electric energy.

6. Conclusions

The present study numerically investigated the heat transfer and pressure drop characteristics of confined liquid metal flow (Prandtl number $Pr = 0.022$) under a strong axial magnetic field past a rectangular cylinder at varying gap height and incidence angle. A literature review revealed that a particularly effective configuration for passively enhancing heat transfer from a duct side wall in a non-MHD flow was the employment of a cylinder with a rectangular cross-section inclined to the oncoming flow, and with the cylinder axis perpendicular to the flow. This study has investigated the side-wall heat transfer enhancement potential of such a vortex promoter in a quasi-two-dimensional MHD duct flow with side-wall heating. A spectral element method was employed to discretise the governing quasi-two-dimensional and modified Navier–Stokes equations over a two-dimensional domain. The effect of gap height ratio G/L_c of a single upright cylinder for $0.8 \leqslant G/L_c \leqslant 3.2$ on heat transfer efficiency was firstly considered. This was followed by an investigation on the effect of cylinder incidence angle γ on heat transfer efficiency for both the optimal efficiency gap height and duct centre-line configurations for $-90^\circ \leqslant \gamma \leqslant 90^\circ$. For each of these investigations, a Hartmann number of $Ha = 200$ and a Reynolds number $Re = 2000$ were employed.

It was found that the thermal efficiency can be improved by offsetting the cylinder at gap height ratios $1.15 \leqslant G/L_c < 2$, with a peak occurring at $G/L_c = 1.5$. Additional benefits in thermal efficiency could be achieved at $G/L_c = 1.5$ by inclining the cylinder at angles $-37.5^\circ < \gamma \leqslant 22.5^\circ, -7.5^\circ \leqslant \gamma < 0^\circ$ and $0^\circ < \gamma \leqslant 15^\circ$, with a global peak efficiency occurring at $\gamma = -37.5^\circ$. For a duct-centred cylinder, additional benefits to thermal efficiency could similarly be achieved by inclining the cylinder to $\gamma = -7.5^\circ$ or $0^\circ < \gamma \leqslant 22.5^\circ$. However, none of these configurations provided benefits greater than simply offsetting an upright cylinder at $G/L_c = 1.5$. It was also found for both cases that increases in mechanical penalties and heat transfer are not always positively correlated.

The location of the global streamwise peak and trough of the time-averaged local Nusselt number were found to be a direct function of the obstacle incidence angle, the distance between the fixed separation points and the *Re* and *Ha* dependent vortex shedding frequency. The time-averaged regions of increased and decreased local heat transport suggest that the irregularity in the thermal response is dominated by the loss of clear vortical structure and wake coherence, rather than the observed time-dependent lateral oscillations.

A net power balance analysis showed that for even modest increases in heating power over pumping power can lead to large increases in net available energy due to the small Prandtl, Reynolds and Eckert numbers found in fusion cooling applications. Analysis of the Hartmann number influence for a representative test case showed a reduction in heat transfer follows an approximate exponential relationship with increased magnetic field strength. Through an order of magnitude analysis, an asymptotic *Nu* in the limit as $Ha \to \infty$ for a fixed *Re* was shown to exist. It was also found that the total duct pressure loss follows a positive linear relationship with increasing Hartmann number. Comparison with the analytical empty duct solution showed the increased pressure penalties due to the addition of a vortex promoter becomes insignificant for moderate to high *Ha*. Moreover, increasing *Ha* generally resulted in a shift of the dominant lift coefficient frequencies to larger values, a narrowing of the peak, and less dispersion of energy across the spectrum.

Acknowledgments

O.G.W.C. was supported by an Engineering Research Living Allowance (ERLA) scholarship from the Faculty of Engineering, Monash University. This research was supported by Discovery Grants DP120100153 and DP150102920 from the Australian Research Council, and was undertaken with the assistance of resources from the National Computational Infrastructure (NCI), which is supported by the Australian Government.

References

[1] J. Sommeria, R. Moreau, Why, how, and when, MHD turbulence becomes two-dimensional, J. Fluid Mech. 118 (1982) 507–518.
[2] J. Moreau, R. Sommeria, Electrically driven vortices in a strong magnetic field, J. Fluid Mech. 189 (1988) 553–569.
[3] I.R. Kirillov, C.B. Reed, L. Barleon, K. Miyazaki, Present understanding of MHD and heat transfer phenomena for liquid metal blankets, Fusion Eng. Des. 27 (1995) 553–569.
[4] A. Pothérat, J. Sommeria, R. Moreau, An effective two-dimensional model for MHD flows with transverse magnetic field, J. Fluid Mech. 424 (2000) 75–100.
[5] R.J. Lingwood, T. Alboussiere, On the stability of the Hartmann layer, Phys. Fluids 11 (1999) 2058–2068.
[6] B. Muck, C. Gunther, U. Müller, L. Bühler, Three-dimensional MHD flows in rectangular ducts with internal obstacles, J. Fluid Mech. 418 (2000) 265–295.
[7] R. Klein, A. Pothérat, Appearance of three dimensionality in wall-bounded MHD flows, Phys. Rev. Lett. 104 (2010) 034502.
[8] J.C.R. Hunt, K. Stewartson, Magnetohydrodynamic flow in rectangular ducts. II, J. Fluid Mech. 23 (1965) 563–581.
[9] D. Krasnov, O. Zikanov, T. Boeck, Numerical study of magnetohydrodynamic duct flow at high Reynolds and Hartmann numbers, J. Fluid Mech. 704 (2012) 421–446.
[10] N. Kanaris, X. Albets, D. Grigoriadis, S. Kassinos, Three-dimensional numerical simulations of magnetohydrodynamic flow around a confined circular cylinder under low, moderate, and strong magnetic fields, Phys. Fluids 25 (2013) 074102.
[11] R. Klein, A. Pothérat, Why, how and when MHD turbulence at low R_m becomes three-dimensional, J. Fluid Mech. 168–205 (2014).
[12] H. Kobayashi, Large eddy simulation of magnetohydrodynamic turbulent duct flows, Phys. Fluids 20 (2008) 015102.
[13] L. Bühler, Instabilities in quasi-two-dimensional magnetohydrodynamic flows, J. Fluid Mech. 326 (1996) 125–150.
[14] M. Frank, L. Barleon, U. Müller, Visual analysis of two-dimensional magnetohydrodynamics, Phys. Fluids 13 (2001) 2287–2295.
[15] A. Pothérat, J. Sommeria, R. Moreau, Numerical simulations of an effective two-dimensional model for flows with a transverse magnetic field, J. Fluid Mech. 534 (2005) 115–143.
[16] A. Pothérat, Quasi-two-dimensional perturbations in duct flows under transverse magnetic field, Phys. Fluids 19 (2007) 074104.
[17] A.H.A. Hamid, W.K. Hussam, A. Pothérat, G.J. Sheard, Spatial evolution of a quasi-two-dimensional Kármán vortex street subjected to a strong uniform magnetic field, Phys. Fluids 27 (2015) 053602.

[18] V. Dousset, A. Pothérat, Characterization of the flow past a truncated square cylinder in a duct under a spanwise magnetic field, J. Fluid Mech. 691 (2012) 341–367.
[19] H. Branover, A. Eidelman, M. Nagorny, Use of turbulence modification for heat transfer enhancement in liquid metal blankets, Fusion Eng. Des. 27 (1995) 719–724. Proceedings of the Third International Symposium on Fusion Nuclear Technology.
[20] H.S. Yoon, H.H. Chun, M.Y. Ha, H.G. Lee, A numerical study on the fluid flow and heat transfer around a circular cylinder in an aligned magnetic field, Int. J. Heat Mass Trans. 47 (2004) 4075–4087.
[21] D. Chatterjee, S.K. Gupta, MHD flow and heat transfer behind a square cylinder in a duct under strong axial magnetic field, Int. J. Heat Mass Trans. 88 (2015) 1–13.
[22] W.K. Hussam, M.C. Thompson, G.J. Sheard, Dynamics and heat transfer in a quasi-two-dimensional MHD flow past a circular cylinder in a duct at high Hartmann number, Int. J. Heat Mass Trans. 54 (2011) 1091–1100.
[23] W.K. Hussam, G.J. Sheard, Heat transfer in a high Hartmann number MHD duct flow with a circular cylinder placed near the heated side-wall, Int. J. Heat Mass Trans. 67 (2013) 944–954.
[24] F. Ying, H. Hulin, Simulation of free surface MHD-flow and heat transfer around a cylinder, Heat Trans. Asian Res. 37 (1) (2008) 11–19.
[25] W.K. Hussam, M.C. Thompson, G.J. Sheard, Optimal transient disturbances behind a circular cylinder in a quasi-two-dimensional magnetohydrodynamic duct flow, Phys. Fluids 24 (2012) 024150.
[26] W.K. Hussam, M.C. Thompson, G.J. Sheard, Enhancing heat transfer in a high Hartmann number magnetohydrodynamic channel flow via torsional oscillation of a cylindrical obstacle, Phys. Fluids 24 (2012) 113601.
[27] T. Alam, R.P. Saini, J.S. Saini, Use of turbulators for heat transfer augmentation in an air duct a review, Renew. Energy 62 (2014) 689–715.
[28] S. Chamoli, N.S. Thakur, J.S. Saini, A review of turbulence promoters used in solar thermal systems, Renew. Sust. Energy Rev. 16 (5) (2012) 3154–3175.
[29] M. Meis, F. Varas, A. Velázquez, J.M. Vega, Heat transfer enhancement in micro-channels caused by vortex promoters, Int. J. Heat Mass Trans. 53 (1–3) (2010) 29–40.
[30] T. Icoz, Y. Jaluria, Design optimization of size and geometry of vortex promoter in a two-dimensional channel, J. Heat Transf. Trans. ASME 128 (10) (2006) 1081–1092.
[31] J. Wang, Pressure drop and flow distribution in parallel-channel configurations of fuel cells: U-type arrangement, Int. J. Hydrog. Energy 33 (21) (2008) 6339–6350.
[32] E.C. Brouillette, P.S. Lykoudis, Magneto fluid mechanic channel flow. I. experiment, Phys. Fluids 5 (1967) 995–1001.
[33] K. Miyazaki, K. Konishi, S. Inoue, MHD pressure drop of liquid metal flow in circular duct under variable transverse magnetic field, J. Nucl. Sci. Technol. 2 (1991) 159–161.
[34] P. Bhuyan, K. Goswami, Effect of magnetic field on MHD pressure drop inside a rectangular conducting duct, IEEE Trans. Plasma Sci. 1955–1959 (2008).
[35] U. Burr, L. Barleon, U. Müller, A. Tsinober, Turbulent transport of momentum and heat in magnetohydrodynamic rectangular duct flow with strong sidewall jets, J. Fluid Mech. 406 (2000) 247–279.
[36] L. Barleon, U. Burr, R. Stieglitz, M. Frank, Heat transfer of a MHD flow in a rectangular duct, in: A. Alemany, P. Marty, J.P. Thibault (Eds.), Transfer Phenomena in Magnetohydrodynamic and Electroconducting Flows: Selected Papers of the PAMIR Conference held in Aussois, France, 22–26 September, 1997, Fluid Mechanics and its Applications, vol. 51, Kluwer Academic Publishers, Aussois, France, 1997, ISBN 978-3-642-03085-7, pp. 305–309.
[37] L. Barleon, U. Burr, K.-J. Mack, R. Stieglitz, Heat transfer in liquid metal cooled fusion blankets, Fusion Eng. Des. 51–52 (2000) 723–733.
[38] V. Dousset, A. Pothérat, Numerical simulations of a cylinder wake under a strong axial magnetic field, Phys. Fluids 20 (2008) 017104.
[39] S. Smolentsev, N. Vetcha, R. Moreau, Study of instabilities and quasi-two-dimensional turbulence in volumetrically heated magnetohydrodynamic flows in a vertical rectangular duct, Phys. Fluids 24 (2012) 024101.
[40] M.A. Hossain, Viscous and Joule heating effects on MHD-free convection flow with variable plate temperature, Int. J. Heat Mass Trans. 35 (1992) 3485–3487.
[41] N.B. Morley, J. Burris, L.C. Cadwallader, M.D. Nornberg, GaInSn usage in the research laboratory, Rev. Sci. Instrum. 79 (5) (2008) 056107.
[42] F. Kreith, M. Bohn, Principles of Heat Transfer, Brooks/Cole Pub., Australia; Pacific Grove, Calif., 2001.
[43] T.A. Myrum, X. Qiu, S. Acharya, Heat transfer enhancement in a ribbed duct using vortex generators, Int. J. Heat Mass Transfer 36 (14) (1993) 3497–3508.
[44] S.J. Yang, Numerical study of heat transfer enhancement in a channel flow using an oscillating vortex generator, Heat Mass Transfer 39 (3) (2003) 257–265.
[45] Y.-Y. Tsui, S.-W. Leu, C.-C. Lin, P.-W. Wu, Heat transfer enhancement by multilobe vortex generators: Effects of lobe parameters, Numer. Heat Transfer 37 (6) (2000) 653–672.
[46] G.E. Karniadakis, M. Israeli, S.A. Orszag, High-order splitting methods for the incompressible Navier–Stokes equations, J. Comput. Phys. 97 (1991) 414–443.
[47] G.J. Sheard, M.P. King, Horizontal convection: Effect of aspect ratio on Rayleigh number scaling and stability, Appl. Math. Mod. 35 (2011) 1647–1655.
[48] S. Smolentsev, C. Wong, S. Malang, M. Dagher, M. Abdou, MHD considerations for the DCLL inboard blanket and access ducts, Fusion Eng. Des. 85 (7–9) (2010) 1007–1011.
[49] E. Mas de les Valls, L.A. Sedano, L. Batet, I. Ricapito, A. Aiello, O. Gastaldi, F. Gabriel, Lead-lithium eutectic material database for nuclear fusion technology, J. Nucl. Mater. 376 (3) (2008) 353–357.
[50] B. Schulz, Thermophysical properties of the li(17)pb(83) alloy, Fusion Eng. Des. 14 (3–4) (1991) 199–205.
[51] K. Pearson, Contributions to the mathematical theory of evolution. II. Skew variation in homogeneous material, Philos. Trans. Roy. Soc. London A 186 (1895) 343–414.